ELSEVIER

Ultramicroscopy 60 (1995) 115–135

ultramicroscopy

Energy-filtering and composition-sensitive imaging in surface and interface studies using HREM

Z.L. Wang *,[1], A.J. Shapiro

Metallurgy Division, National Institute of Standards and Technology, Building 223, Gaithersburg, MD 20899, USA

Received 1 December 1994; in final form 17 February 1995

Abstract

Energy-filtered high-resolution electron microscopy (HREM) is an important technique for quantitative structural determination. In this paper, some fundamental quantities in applying energy-selected HREM in surface and interface studies are considered. The inelastic absorption function in zero-loss energy-selected HREM profile images of the MgO(100) surface is measured. The inelastic scattering mean-free-path length of MgO at 300 kV is determined as $\Lambda \approx 181$ nm for [110] zone-axis diffraction condition with an objective aperture of semi-collection angle 1 Å^{-1}. High-resolution chemical-sensitive imaging using core-shell loss electrons in transmission electron microscopy (TEM) is also demonstrated in studies on Al/Ti multilayer thin films. A spatial resolution of ~ 0.4 nm has been obtained. It has been shown that the spatial resolution of energy-selected ionization edge electron images is dominated by the signal-to-noise ratio; the signal localization, as long as it comes from inner-shell excitation, has little effect. Thus, for a general element, the use of low loss ionization edges rather than higher loss ionization edges is recommended for forming chemical images. But caution must be exercised in the subtraction of background due to the influence of multiple plasmon peaks. Composition-sensitive imaging using plasmon-loss electrons is also feasible, and a spatial resolution better than 1.0 nm has been obtained. These results are interpreted using the calculations of the dielectric response theory for interface excitation. Lattice images formed by plasmon-loss and multiple plasmon-loss electrons are also illustrated.

1. Introduction

Obtaining reliable structural information from materials at atomic resolution is one of the major research fields of high-resolution electron microscopy (HREM). Various techniques have been developed to extract quantitative information from HREM images. Traditional methods have relied upon qualitative comparisons between experimental micrographs and image simulations based upon structural models, with the acceptability of the particular model being considered as improved if an image "match" is obtained for several members of a through-focal series [1]. Iteration between calculations and experimental images based upon least-squares refinement methods may significantly improve the accuracy of the quantification. Approaches which combine image and diffraction pattern information, such as maximum entropy methods [2], have shown

* Corresponding author. Fax: +1 404 853 9140; E-mail: zhong.wang@mse.gatech.edu.

[1] Currently at: School of Materials Science and Engineering, Georgia Institute of Technology, Atlanta, GA 30332-0245, USA.

0304-3991/95/$09.50 © 1995 Elsevier Science B.V. All rights reserved
SSDI 0304-3991(95)00042-9

some new possibilities. For all these studies, however, HREM images have been recorded without using an energy filter, so that both the elastically and inelastically scattered electrons contribute to the image. This makes quantitative data analysis difficult because only the scattering of elastic electrons can be accurately simulated using existing dynamical theories. An energy filter can remove all the inelastically scattered electrons except those scattered by phonons, since the energy loss, typically about 0.08 eV, is much less than the resolution of the filter.

There are two methods to performing energy filtering in transmission electron microscopy (TEM). One method uses a Castaing–Henry filter [3]. The Castaing–Henry filter consists of two 90° magnetic prisms and a retarding electric field. The filter is located between the objective lens and the intermediate lens. The electrons are sent to a 90° electromagnetic sector, and then they are reflected by an electrostatic mirror. The electrons having different energies are dispersed. The second 90° prism deflects the electron back onto the optic axis. A slit is placed before the intermediate lens and selects the electrons with specific energy losses. With this system, either the energy-filtered diffraction pattern or image is formed by the intermediate lens and projection lens as in conventional electron optic systems. The Castaing–Henry filter is unsuitable for primary beam voltages greater than about 100 kV. The filter designed by Senoussi et al. [4] is a better choice for higher energy electrons. This energy filtering can only be performed on a specially built TEM. A detailed introduction of this energy-filtering system and its applications has been given by Reimer and coworkers [5–7]. The detection limits of this technique for chemical-sensitive imaging has recently been considered by Berger et al. [8].

The other energy-filtering method uses the parallel-detection electron energy-loss spectroscopy (PEELS) system [9,10]. The electrons are dispersed by the magnetic sectors in the EELS spectrometer. An energy-selecting slit is introduced at the exit face of the EELS spectrometer to select the electrons with particular energy losses. A set of lenses are then arranged to re-disperse the electrons and re-form the image (or diffraction pattern) using the energy-selected electrons. The final image/diffraction pattern is recorded digitally using a charge-coupled device (CCD) camera. This energy-selecting system can be equipped to any existing TEMs without any modification to the electron optics. More importantly, energy-filtering of high-resolution images can be performed using this method.

In this paper, we first show energy-filtered HREM images of MgO cubes obtained using zero-loss (elastically scattered) electrons (Section 3.1). The inelastic scattering mean-free-path length (Λ) is measured from the filtered image intensity. In Section 3.2, the localization effect of inelastic surface excitation in surface profile imaging will be examined. The dependence of the absorption function $\mu = 1/\Lambda$ on impact distance from the surface is shown in the energy-filtered profile images of MgO(100). In Section 3.3, composition-sensitive imaging using electrons with characteristic energy losses of the ionization edges are illustrated. A spatial resolution of ~ 0.4 nm has been achieved. Then, composition-sensitive images formed by valence (or plasmon) loss electrons are demonstrated (Section 3.4), and a spatial resolution better than 1.0 nm is obtained. It is shown that plasmon-loss and multiply scattered valence-loss electrons can also form HREM lattice images. Finally, the dielectric response theory of interface excitation is applied to interpret the observed spatial resolution (Section 4).

2. Inelastic excitations and energy-filtering

The goal of an energy filter is to form images (or diffraction patterns) using electrons with specific energy losses. The interaction between an incident electron and the atoms in condensed matter results in various inelastic scattering processes [11]. First, thermal diffuse scattering or phonon scattering is the result of atomic vibrations in crystals. This process does not introduce any significant energy loss (< 0.1 eV) but produces large momentum transfer. Second, valence-loss (or plasmon for metals and semiconductors) excitation, which characterizes the transitions of electrons from the valence band to the

conduction band, involves an energy loss in the range of 1–50 eV. Third, atomic inner-shell ionization is excited by the energy transfer of the incident electron, resulting in an ejected electron from the deep-core states. This process is a signature of the corresponding element, thus, it can be applied to form composition-sensitive images.

There are two continuous energy-loss processes in electron scattering. Continuous energy-loss spectra can be generated by an electron which penetrates into the specimen and undergoes collisions with the atoms in it. The electromagnetic radiation produced is known as Bremsstrahlung, leading to continuous energy loss that increases with increasing scattering angle. X-rays are usually generated. The other process is the energy transfer due to collision of the incident electron with an electron belonging to the specimen. This process is known as electron Compton scattering or electron–electron (e–e) scattering. Electron Compton scattering leads to large losses (a broad peak from a few tens of eV to several hundred eV) with a peak that moves to high energy losses for increasing scattering angle.

In an electron energy-loss spectrum, the zero-loss peak is composed of elastically and thermal diffusely scattered electrons. The low-loss region is dominated by valence excitations. Atomic core-shell excitations usually produces energy losses from a few tens of eV to a few thousand eV, depending on the binding energy of the core electron. The background observed in EELS is produced by scattering processes of multiple valence excitations, electromagnetic radiation and e–e scattering (or electron Compton scattering). For composition-sensitive imaging, the background due to continuous energy losses must be subtracted.

The HREM experiments were performed using an JEOL 3010 HREM (300 kV) with a point-to-point image resolution of 0.167 nm. The microscope is equipped with the Gatan imaging filtering (GIF) system that allows both parallel-detection EELS and energy-filtered imaging/diffraction. A CCD camera, placed at the end of the energy-filtering system, allows digital recording of electron images and diffraction patterns at 1024 × 1024 pixels resolution. The recorded image can be processed using a variety of image-processing softwares.

When forming images using electrons that have suffered an energy loss ΔE, an additional focus shift of $\Delta f_c = C_c \Delta E / E_0$ is introduced with respect to the zero-loss energy-filtered image due to chromatic aberration effect; here C_c is the chromatic aberration coefficient of the objective lens and E_0 the primary beam energy. Thus, the total defocus value is $\Delta f = \Delta f_{obj} + \Delta f_c$, where Δf_{obj} is the defocus of the objective lens. Since C_c is typically about 2 mm, $\Delta f_c = 100$ nm for energy loss $\Delta E = 15$ eV. This defocus shift, caused by chromatic aberration, is sufficiently large to produce either contrast reversal or contrast smearing. Thus, a mechanism, described below, is introduced in the design of the GIF controlling system in order to record an "in-focus" (with respect to the zero-loss image) energy-filtered image.

When an energy-selected image is formed with electrons that have experienced no energy loss (elastic image), the imaging filter selects electrons of the primary energy E_0. If the primary energy is then increased by ΔE, but everything else is kept the same, the new image formed by the electrons that have suffered an energy loss ΔE will still be formed with electrons of energy E_0, having the same defocus as the elastic image. Since the energy of the imaging electrons is not changed, the objective lens does not need to be refocused. Since it would be unwise to increase the high voltage of the TEM above its maximum operating value, the GIF control of the microscope primary energy is connected in such a way that it can only decrease the primary energy. This idea was originated by Colliex [12]. This means that under normal operation, the beam energy is automatically lowered by 2 kV as soon as the GIF system is turned on, and then increased by ΔE as needed for energy-selecting to reach energy losses up to 2 keV high. Therefore, the microscope was operated at voltages from 298 to 300 kV. Independent of the mode and magnification of the microscope, the GIF system allows only 3 mm diameter illuminated area at the position of the microscope viewing screen to be recorded.

In this paper, surface profile imaging is stud-

ied using MgO cubes, with edge dimensions of about 200 nm. The cubes were collected on holey carbon films from MgO smoke while burning an Mg ribbon in air. The interface studies were carried out using cross-sectional Ti/Al multilayer samples, which were prepared by vapor deposition. The layer thickness is about 50 nm. The width of energy-selecting slit was chosen as 8 eV for most of data acquisitions. For Ti-L edge, the energy window was chosen as 20 eV in order to get enough intensity. For all the data acquisition, the dose rate was 0.2–0.4 pA/nm^2.

3. Experimental results

3.1. HREM using zero-loss electrons

An important application of the energy filter is to form HREM images using electrons without energy loss, i.e. purely elastically and quasi-elastically (i.e. phonon) scattered electrons. Accurate structure determination is feasible using these images, since image simulations can be done accurately based on elastic scattering theory. The GIF system allows recording energy-selected atomic resolution images. Two factors can be assessed from this study: (1) the contribution of inelastically scattered electrons to HREM images; and (2) the effect of absorption by inelastic scattering on images obtained using zero energy-loss electrons.

Fig. 1 shows a pair of MgO lattice images recorded using all the transmitted (Fig. 1a) and only elastically transmitted (Fig. 1b) electrons, respectively. The MgO cube is oriented along [110], so that the contrast variation as a continuous function of the specimen thickness, from zero (at the top) to 33 nm (at the bottom), is revealed by a single image. The local thickness is twice the distance measured from the wedge of the cube in the image. When the specimen is thinner than about 20 nm, no significant differences are seen between the filtered and unfiltered images. In the unfiltered image, the image contrast is dramatically decreased when the specimen thickness is about 40 nm (as indicated by an arrowhead), but the zero-loss filtered image shows significantly better contrast. Quantitative calculation has shown that the high-resolution phase contrast is improved from 7% to 11% when the image filter is applied. The advantage of energy-filtering is pronounced particularly when the specimen thickness is large, as seen at the bottom of Fig. 1. Although the intensity in the filtered image drops due to inelastic absorption (see below), the image contrast is improved significantly. This allows structure determination from specimen areas with larger thicknesses. Our results here demonstrate the improvement of high-resolution phase contrast when the energy-filtering is applied. Theoretical and experimental evaluations on the improvement of low-resolution image contrast with the use of an energy filter have given be Reimer and co-workers [13,14].

We now look at the zero-loss image and try to extract some useful information. In TEM imaging, the energy-loss distribution of all the transmitted electrons is described by Poisson's law [15]

$$J(\Delta E) = \exp(-d/\Lambda) \sum_{n=0} \frac{(d/\Lambda)^n}{n!}\{f_E\}_n$$
$$= \exp(-d/\Lambda) + \exp(-d/\Lambda)(d/\Lambda) f_E$$
$$+ \exp(-d/\Lambda)\frac{(d/\Lambda)^2}{2!}\{f_E \otimes f_E\} + \cdots \quad (1)$$

with

$$\{f_E\}_n = \{f_E \otimes \cdots \otimes f_E\}_n, \quad (2)$$

f_E is the single-loss function, $\otimes$ stands for energy convolution calculation and d is the specimen thickness. In Eq. (1), the first term is the zero-loss intensity, which decreases with increasing specimen thickness in agreement with the observation shown in Fig. 1b. The second term is the first order valence (or plasmon) excitation, the third term being the second order plasmon excitation. It can be directly proven from Eq. (1) that

$$\int_0^\infty \mathrm{d}\Delta E\, J(\Delta E) = 1, \quad (3)$$

Eq. (3) means the conservation of the total electron intensity. Theoretically, the intensity of the zero-loss energy-filtered image is related to the local specimen thickness by

$$J_0 = \exp(-d/\Lambda) = I_0/I, \quad (4)$$

where I_0 and I are the average intensities of the zero-loss filtered and unfiltered images, respectively. Since the local thickness of MgO can be directly measured from the image owing to its cubic shape, and I_0 and I can be directly determined from the images recorded with and without energy-filtering, respectively, Eq. (4) can be applied to measure the inelastic mean-free-path length Λ.

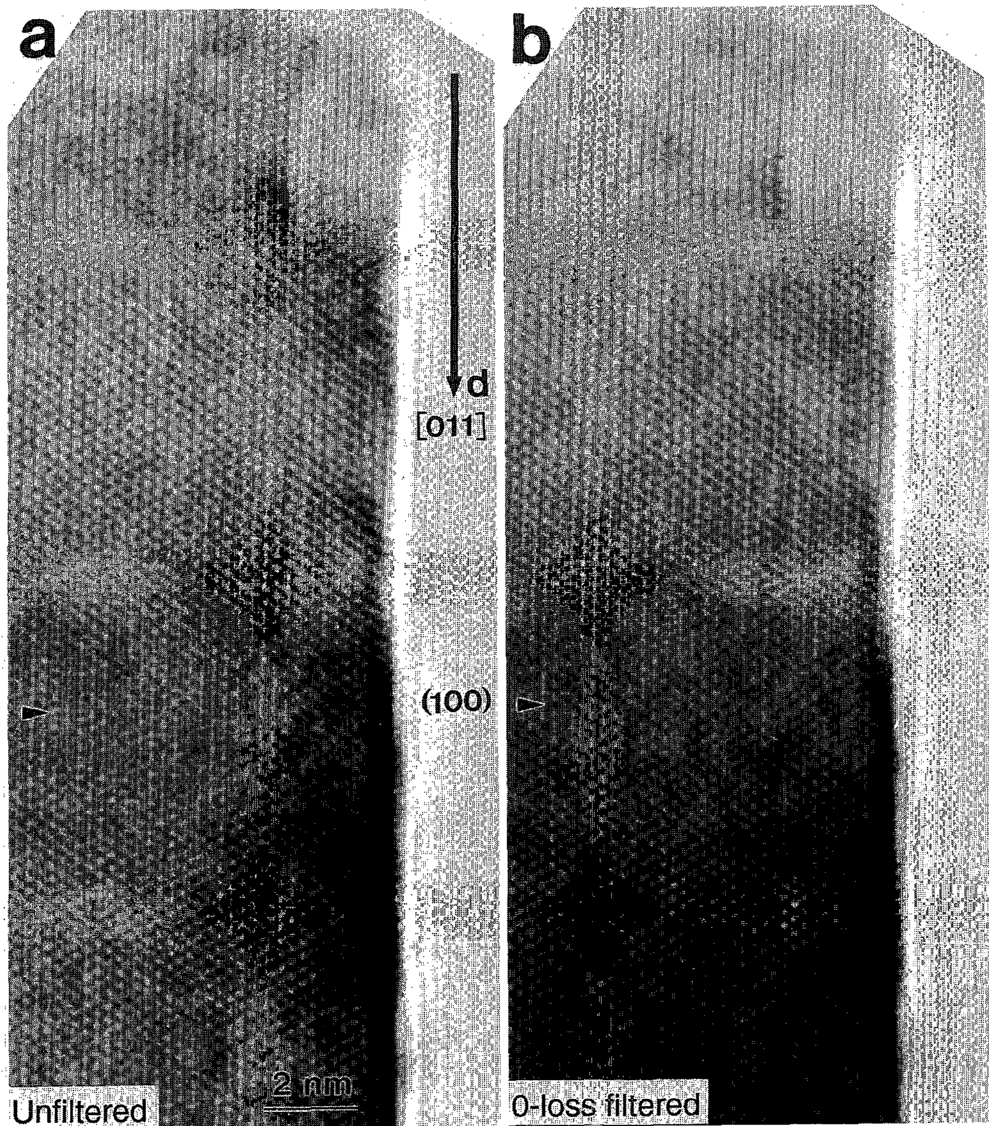

Fig. 1. Energy unfiltered (a) and zero-loss filtered (b) HREM profile images of MgO(100) surface, oriented along [01$\bar{1}$]. The specimen thickness increases linearly from zero along the direction indicated.

Fig. 2 shows a plot of I_0/I as a function of specimen thickness d. This curve was obtained by dividing the intensity of the image formed by the zero-loss electrons (Fig. 1b) by that of the image formed by the entire transmitted electrons (Fig. 1a). An intensity line scan is made along [011], parallel to which the specimen thickness increases linearly. If $d/\Lambda \ll 1$, from Eq. (4), $I_0/I \approx 1 - d/\Lambda$, thus, the slope of the $I_0/I \sim d$ curve is $(-1/\Lambda)$. The measurement from Fig. 2 gives $\Lambda \approx 181$ nm for MgO at 300 kV. This value was measured for zone-axis electron diffraction condition for an objective aperture of radius 1 $Å^{-1}$.

3.2. *Energy-filtered surface profile images*

Determining surface and interface microstructures is important in materials research. Currently HREM is the only technique that can directly reveal the atomic structure of interfaces in real space. In HREM, atomic structures of crystal surfaces can be imaged if the surface is parallel to the incident beam. This is the surface profile imaging technique [1]. We choose MgO (100), which is atomically flat. When viewing along $[01\bar{1}]$, the specimen thickness increases linearly along [011], but is constant along [100]. Thus the contrast variation along [100] can be used to study the surface excitation as the function of the electron impact distance from the surface. Experimental results will be shown in this Section, the corresponding theoretical analysis will be given in Section 4.1.

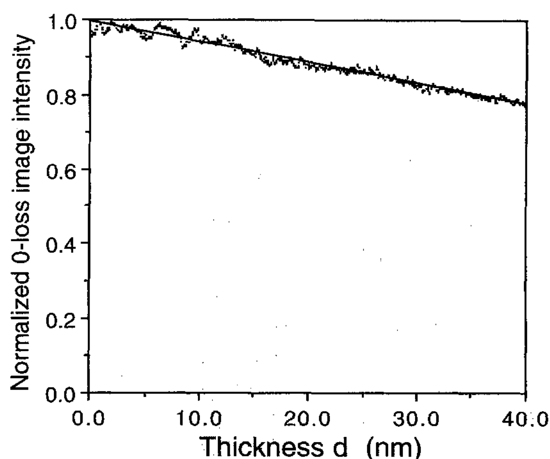

Fig. 2. Normalized zero-loss electron intensity (I_0/I) as a function of specimen thickness. This plot was obtained from the experimental data shown in Fig. 1 after some statistical average. Objective semi-collection angle is 1.0 $Å^{-1}$.

Figs. 3a and 3b compare the unfiltered and zero-loss filtered $[01\bar{1}]$ profile images of MgO (100) surface, respectively. The contrast in the filtered image is slightly better than that of the unfiltered image. For accurate image processing, the intensity of each pixel corresponding to areas in vacuum far from the surface is normalized to 1 in order to remove the statistical fluctuation of electron arriving rate. The intensity variation at the top surface layer results from Fresnel fringes [16].

The subtraction of the intensity of the zero-loss filtered image (Fig. 3b) from that of the unfiltered image (Fig. 3a) gives the image formed by all the inelastically scattered electrons, as shown in Fig. 3c. The arrowhead indicates [100]. In this subtraction process, caution must be taken in order to correct the specimen drift between the recording of the two images. This is done with reference to a characteristic feature appearing in both the images. Although the contrast of Fig. 3c is poorer than the zero-loss image, crystal lattices can still be resolved. The contrast smearing results from the energy spreading of the inelastically scattered electrons due to chromatic aberration.

To see the variation of absorption function $1/\Lambda$ near the surface as a function of the electron impact distance from the surface, Fig. 3d shows the processed image of I_0/I obtained by dividing the intensity of the zero-loss image by that of the unfiltered image. The results of an intensity line scan along [100] (as indicated in Fig. 3d) normal to the surface is shown in Fig. 4, where the output values were averaged over a width of 100 pixels parallel to the surface. Disregarding the intensity variation at the edge of the surface due to Fresnel fringes [16], the average intensity profile drops slightly when the beam impact distance approaches the surface, indicating less inelastic absorption near the surface. The

interpretation of this phenomenon will be given in Section 4.1.

A clear fact shown above is the absorption introduced by inelastic scattering. The absorption function drops continuously when the electron approaches the surface. Therefore, a proper ab-

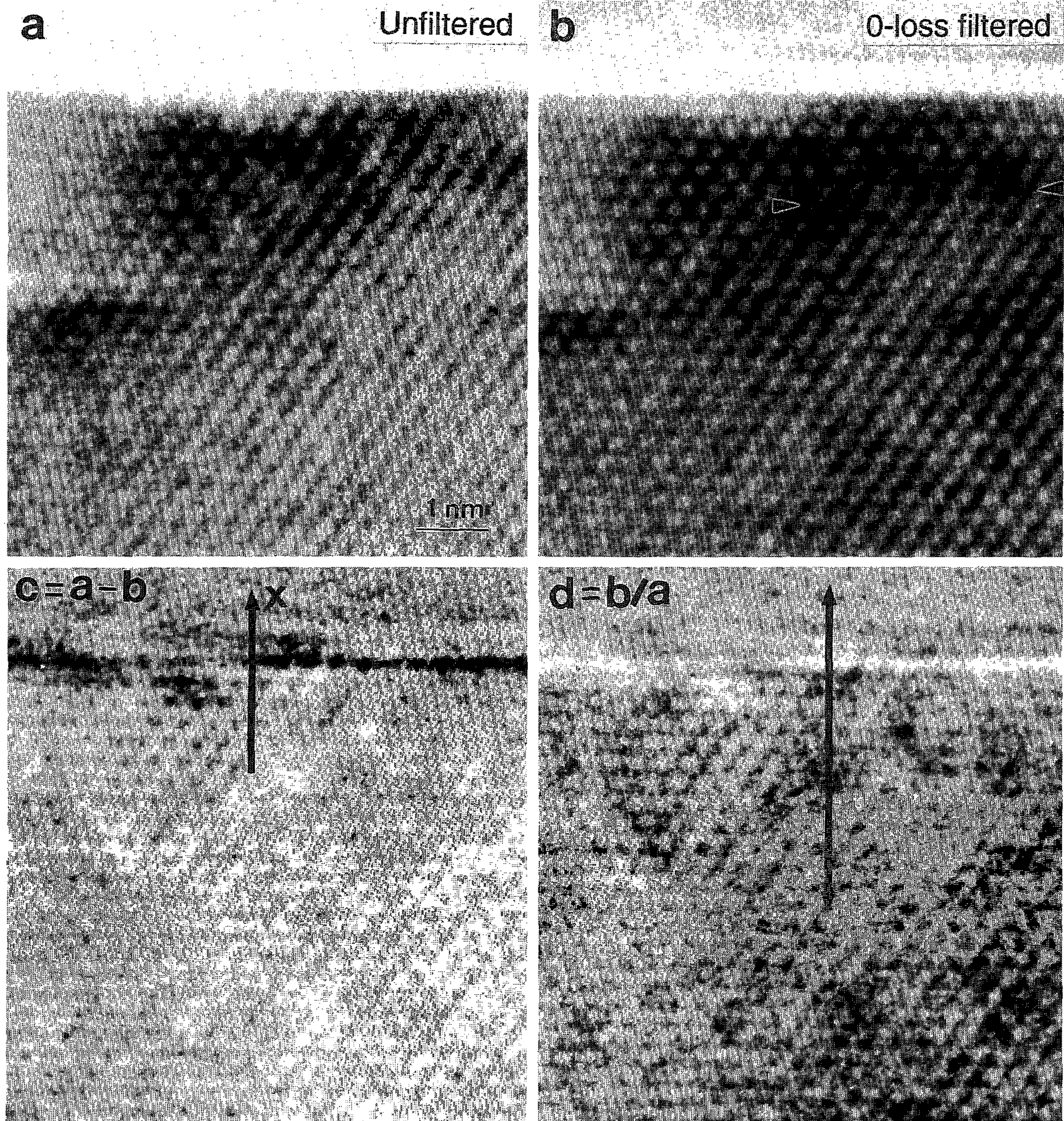

Fig. 3. Energy unfiltered (a) and zero-loss filtered (b) HREM profile images of MgO(100), oriented along [011]. (c,d) Processed images formed by the entire inelastically scattered electrons and the normalized zero-loss electrons (I_0/I), respectively; (c) is a distribution of inelastic absorption function. A stacking fault and the associated partial dislocation are indicated by an arrowhead in (b).

sorption function has to be introduced in the image calculation in order to simulate the zero-loss energy-filtered images.

3.3. Composition-sensitive imaging using core-shell scattered electrons

Compositional imaging at high spatial resolution is vital for solving problems in materials science. There are four basic methods for obtaining composition-sensitive images. In scanning transmission electron microscopy (STEM), inelastically excited signals, such as X-rays and Auger electron emissions, are acquired sequentially as a function of electron scanning position [17,18]. A two-dimensional display of the acquired signal intensity gives a distribution map of the corresponding element. Backscattered electrons in STEM (or scanning electron microscopy) gives a composition-sensitive image because the atomic backscattering factor is directly proportional to the atomic number Z. High-angle annular dark-field imaging (HAADF) in STEM and high-angle hollow-cone dark-field TEM (HADF-TEM) provide chemical images of a specimen [19,20], because the intensity of high-angle phonon-scattered electrons is also related to atomic number Z. Energy-selected electron images correspond to atomic inner-shell ionization edges also allow chemical-sensitive imaging in STEM [21,22] and TEM [9].

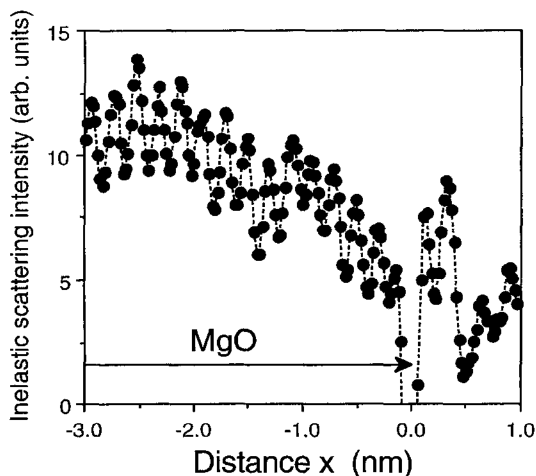

Fig. 4. A plot of the line scan intensity across the MgO(100) surface, as indicated in Fig. 3c, showing the variation of the absorption function across the surface. The intensity oscillation at the surface ($x = 0$) is due to Fresnel fringes.

Using the GIF system it is feasible to obtain chemical images of a specimen at high spatial resolution. Since the ionization signal of the atomic inner shell usually sits on a strong background in EELS, three energy-selected images are usually recorded from each specimen area in order to retrieve the chemical image. Typically, two images are from the pre-edge electrons in order to evaluate the background, and the third image is formed by the electrons when the energy-selecting slit is positioned at the element ionization edge. A numerical processing of these images according to the method introduced in Ref. [9] gives a distribution map of the element. However, it must be pointed out that this three-window technique may not be accurate for low energy-loss ionization edges because of the non-exponential shape of spectrum background owing to the peaks of multiple plasmon excitation.

Fig. 5a is a zero-loss HREM image of an Al/Ti interface, and Figs. 5b–5d are the corresponding background-subtracted chemical-sensitive images obtained using the electrons corresponding to different ionization edges of Al and Ti, respectively. A dislocation line, which is located at the twin boundary of two Al grains, is seen in Fig. 5a. The Ti layer is at the right-hand side. The Al and Ti layers have twin relationship. As reported by Shechtman et al. [23], the Ti layer has transformed from hexagonal close packing to face centered cubic structure after being thinned by ion milling. The interface as seen in the zero-loss image (Fig. 5a) is not sharp. Diffraction contrast due to interface mismatch and stress makes the interface appears broad. Fig. 5b is an energy-selected image of the interface using the Al-$L_{2,3}$ edge electrons with energy losses from 73 to 83 eV, where the Al layer is clearly resolved. The change of contrast in the image reflects the variation of the projected (or thickness integrated) local density of Al, provided the background is properly subtracted. The image (Fig. 5c) recorded using the Ti-$L_{2,3}$ edge, located at energy loss of

455 eV, shows the distribution of Ti. The image formed by the Ti-M edge, located at energy loss about 40 eV, also clearly reveals the existence of the Ti layer (Fig. 5c). The Ti distribution given by the two images is consistent, in that the high Ti concentration seen at the up-right corner of Fig. 5d is also shown at the same region in Fig. 5c.

Theoretically, the Ti-L edge is considered to

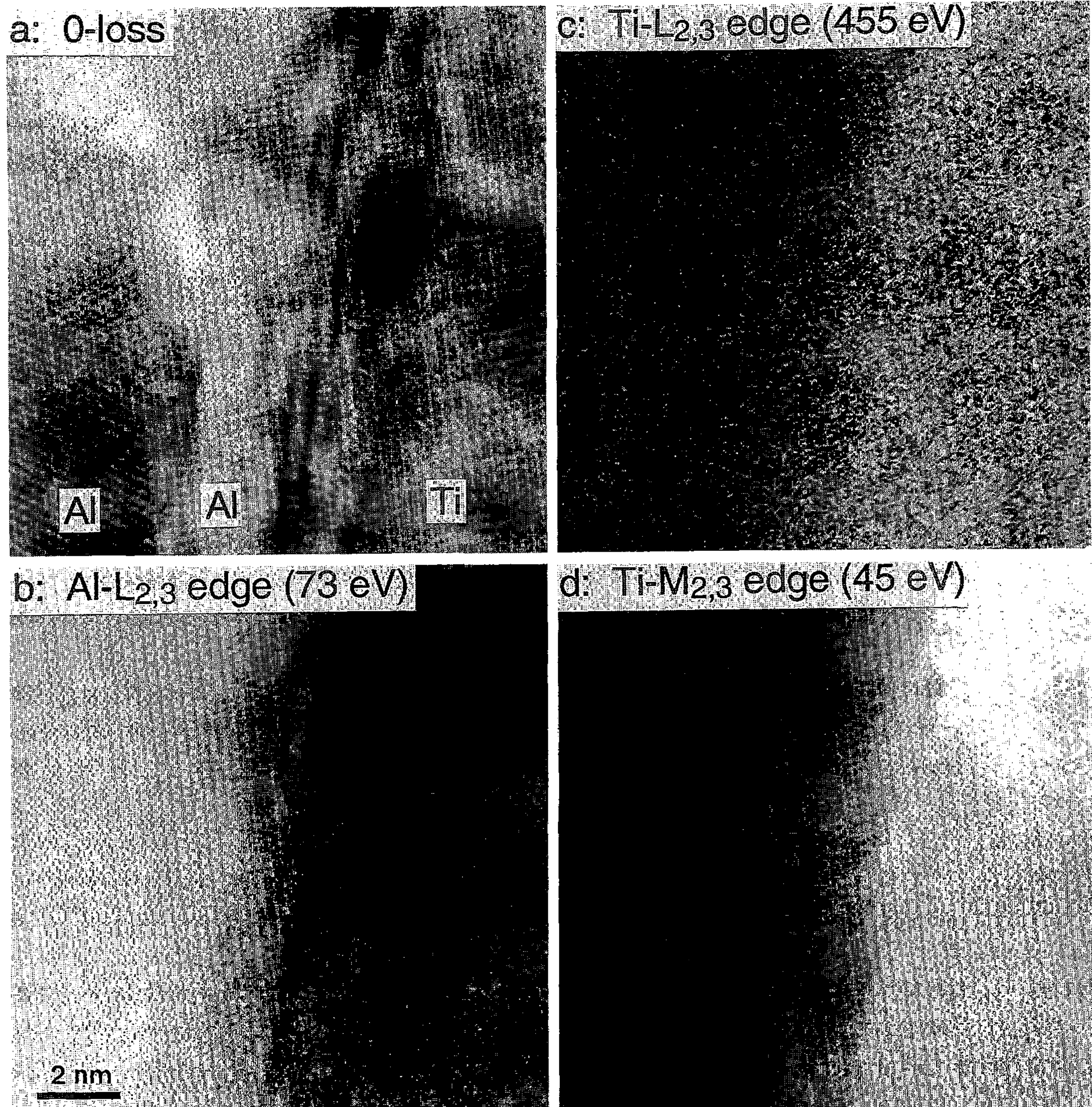

Fig. 5. (a) Zero-loss, (b) background-subtracted Al-$L_{2,3}$ edge ($\Delta E = 73$ eV), (c) background-subtracted Ti-$L_{2,3}$ edge ($\Delta E = 455$ eV) and (d) Ti-$M_{2,3}$ edge ($\Delta E = 40$ eV) energy-selected HREM images of an Al/Ti (111) interface. Crystal structure is clearly seen in the zero-loss image. The composition map is provided by (b)–(d). Beam azimuth [$1\bar{1}0$].

be a much more localized scattering than the Ti-M edge, thus a better spatial resolution is expected to be given by the image formed by the Ti-L edge, in contrast to the experimental results shown in Figs. 5c and 5d. This remarkable result indicates that, as long as the selected electrons come from the inner-shell ionization with either lower or higher energy losses, the spatial resolution is mainly affected by the signal-to-noise ratio. One possible method to improve the signal-to-noise ratio is to increase the width of the energy filter. However, the chromatic aberration in this case is a vital factor which limits the image spatial resolution.

It is important to point out that the presence of diffraction contrast has little effect on the core-loss energy-filtered images. Thus, the diffraction contrast is seen in Fig. 5a, but not in Figs. 5b and 5d. In these ionization energy-filtered images, the image contrast is proportional to the projected number of atoms characterized by the selected ionization edges, respectively. Thus, each energy-selected core-loss electron image provides a thickness integrated chemical image of the specimen if the background image is properly subtracted.

3.4. Composition-sensitive imaging using valence-loss electrons

In chemical-sensitive imaging using core-loss electrons, the signal-to-noise ratio becomes worse if the ionization edge is located at higher energy losses. Therefore, enhancing the signal-to-noise ratio is the most important step for obtaining chemical images using inner-shell ionization edges. For this reason, we explore the possibility of using plasmon-loss electrons for chemical-sensitive imaging. In this Section, we show the compositional information carried in plasmon energy-selected electron images. The observed spatial resolution will be interpreted based on the dielectric response theory given in Section 4.2.

Fig. 6a shows a comparison of the plasmon-loss EELS spectra obtained from the Al and Ti layers, respectively. The Al plasmon peak is located at 15 eV and the Ti plasmon peak at 21 eV. When the EELS spectrum is acquired from both the Al/Ti layers (Fig. 6b), the Al plasmon is a sharp peak centered at 15 eV energy loss, and the shoulder peak at 21 eV energy loss is the plasmon loss of the Ti layer. If an energy-selecting window is set at 15 and 21 eV, the images formed will display the regions that correspond to Al and Ti, respectively.

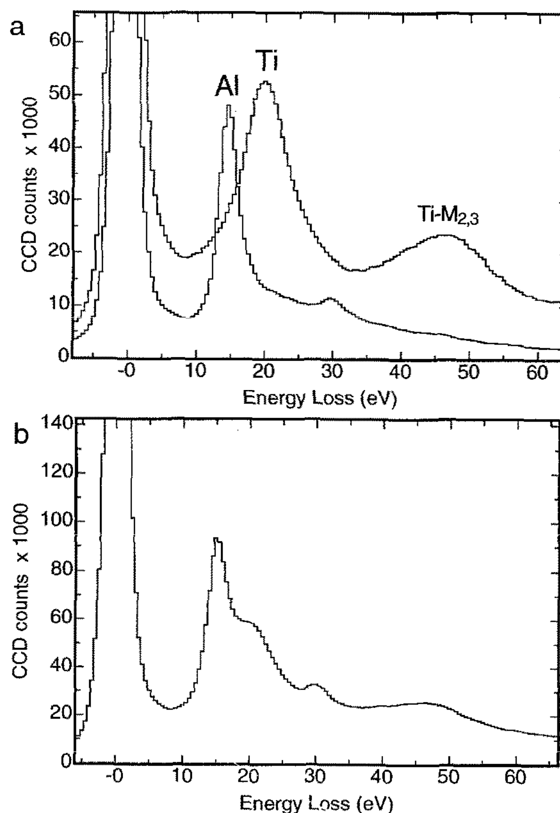

Fig. 6. (a) EELS spectra acquired from the Al and Ti layers, showing the plasmon peaks for Al and Ti. The Ti-$M_{2,3}$ edge is also shown in the spectrum. (b) An EELS spectrum recorded from the transmitted electrons at the Al/Ti interface.

Fig. 7 shows a group of images of the zero-loss (Fig. 7a), Al plasmon (Fig. 7b) and Ti plasmon (Fig. 7c) energy-selected electrons. It is apparent that the Al layer and Ti layer show bright contrast in Figs. 7b and 7c, respectively, which represent high local atomic concentrations. Two advantages are seen in the plasmon-loss energy-selected images. The plasmon-loss intensity is

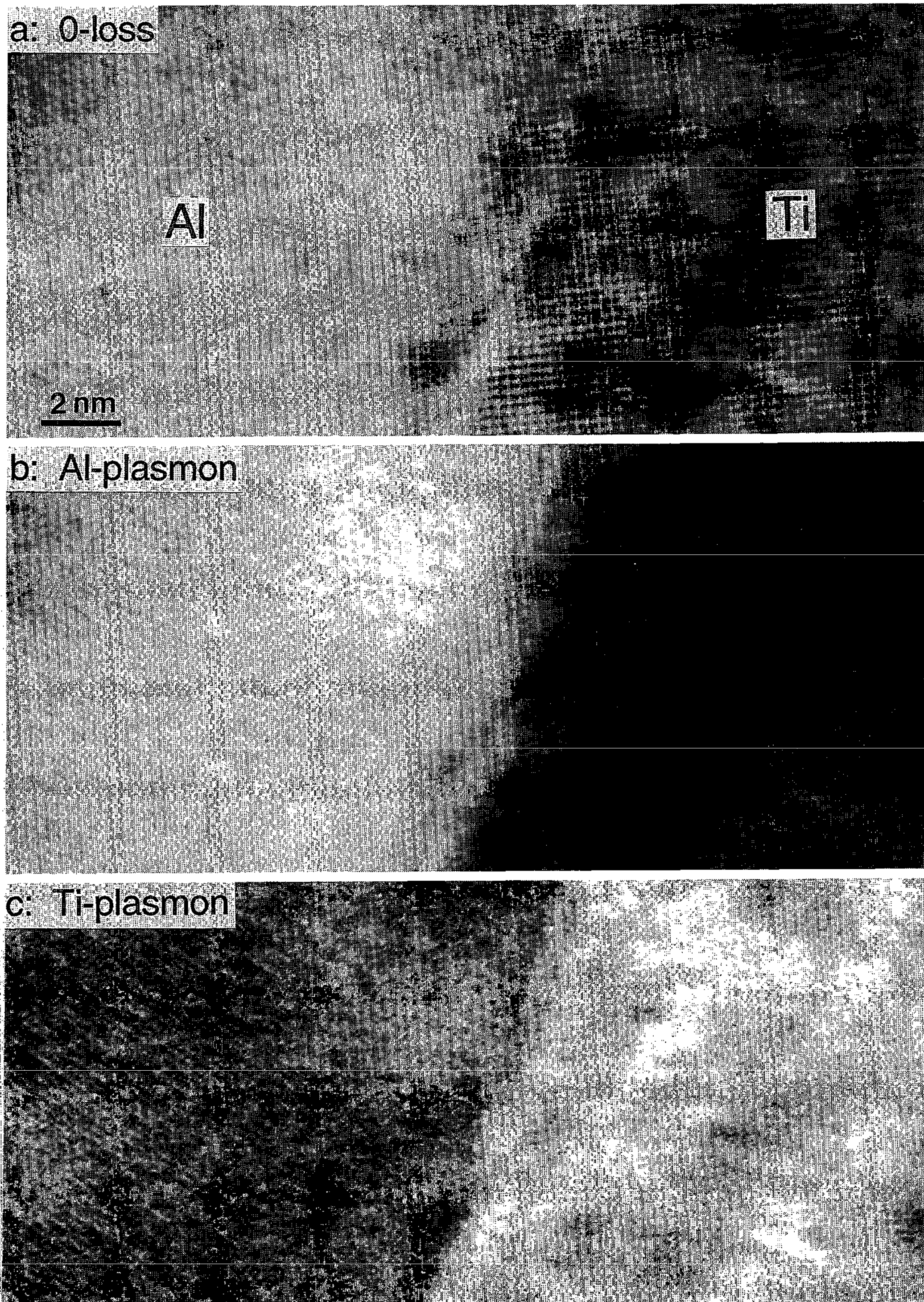

Fig. 7. (a) Zero-loss, (b) Al plasmon ($\Delta E = 15$ eV) and (c) Ti plasmon ($\Delta E = 22$ eV) energy-selected HREM images of an Al/Ti (111) interface, showing the composition sensitivity. But the image contrast is largely influenced by diffraction contrast effect.

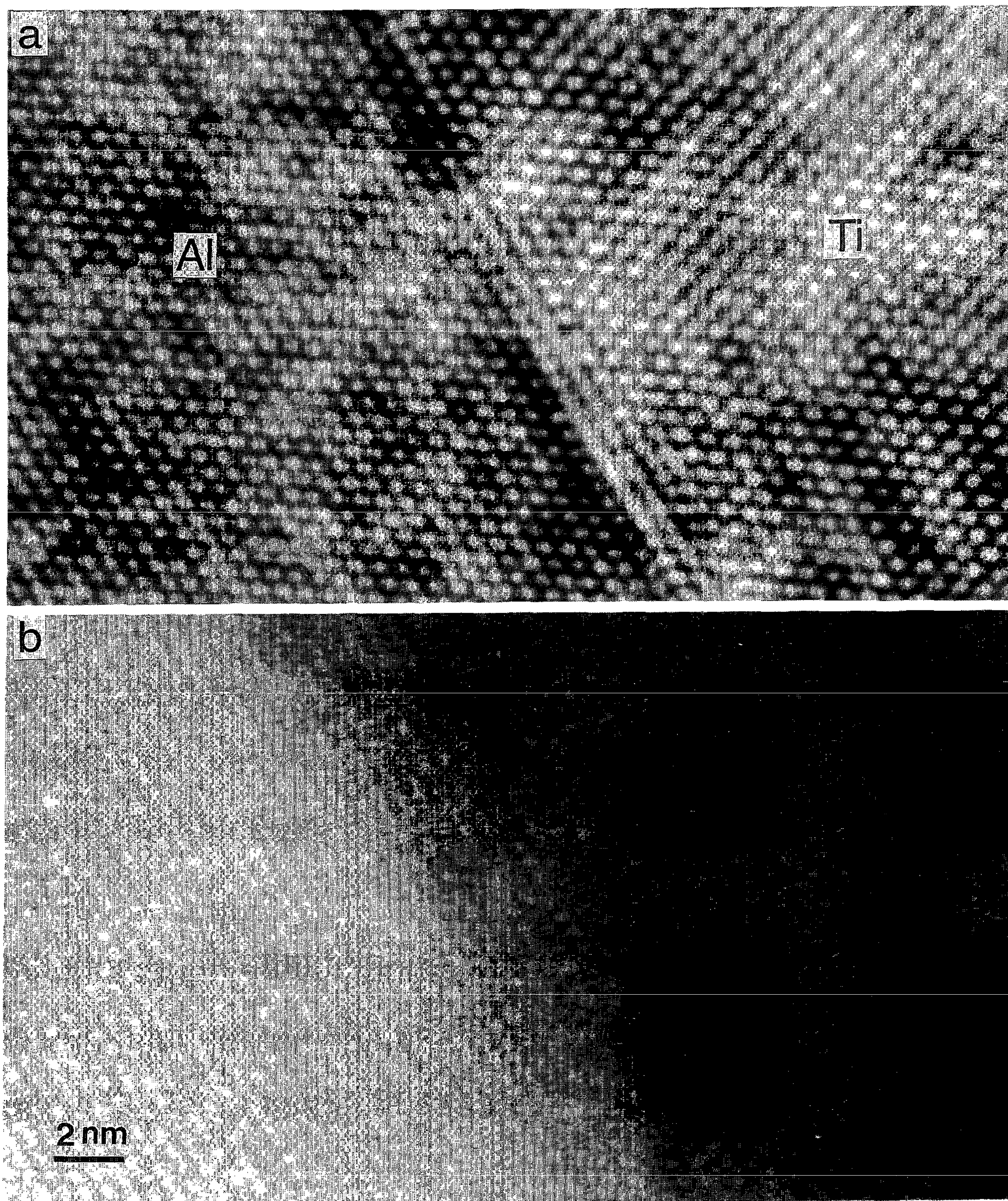

Fig. 8. (a) Zero-loss and (b) 15 eV Al plasmon loss energy-selected HREM images of an Al/Ti (111) interface, showing the formation of lattice images by plasmon-loss electrons. Energy window $\Delta = 4$ eV. Beam azimuth [1$\bar{1}$0].

much larger than the core-shell loss intensity, thus, the image shows better signal-to-noise ratio. The influence of background in valence-loss region is negligible, but it is strong in the energy-loss region of core-shell ionization edges. Thus, data processing is more important in the latter case.

It must be pointed out, however, the energy-selected plasmon-loss image may not be sensitive to the local chemistry if there are strong overlaps in the energy-loss spectra. This occurs for most non-metallic materials. As seen in Fig. 7b, for an example, the intensity seen at the Ti side is due to the stronger overlap of Ti peak with the energy-selecting region.

A comparison of the images formed by zero-loss (Fig. 7a) and plasmon-loss electrons (Figs. 7b and 7c) shows the preservation of diffraction contrast. The dark contrast patches seen in the zero-loss image are seen in the energy-selected plasmon-loss images. This result agrees with the early theory of Howie [24]. Since plasmon loss is a very small angle scattering process, the column approximation assumed in diffraction contrast calculation holds. Also diffraction contrast is less sensitive to a small change in the lens focus. It must be pointed out, however, that the phase contrast, which carries high-resolution information, is not exactly preserved in the plasmon-loss image due to chromatic aberration effect, as pointed out earlier by Wang and Bentley [25]. Lattices are still resolved in the image formed by plasmon-loss electrons, but the contrast variation may not show the same profile as the zero-loss electrons image.

The preservation of diffraction contrast in plasmon-loss images can greatly influence the interpretation of the image contrast. Thus, the overall image intensity is a representation of the average chemical composition, but the local image contrast depends sensitively on the presence of defects, or more generally, strain.

3.5. HREM of plasmon-loss electrons

Using the energy filter, HREM lattice images of crystals can be formed with electrons that have suffered energy losses in a well defined, narrow band due to inelastic interactions with the crystal. Theoretical calculations have shown that significant details can be introduced in the images by the plasmon-loss electrons, particularly when grain boundaries are present [25,26]. Figs. 8a and 8b show a pair of HREM images of an Al/Ti (111) interface recorded using zero-loss and Al plasmon-loss electrons, respectively. It is apparent that the crystal lattice fringes are resolved in the image recorded using the inelastically scattered electrons, although the image contrast is not exactly preserved in comparison to the zero-loss electron image (Fig. 8a). Thus, the overall contrast of the plasmon-loss energy-selected image may provide composition-sensitive information, but the lattice fringes are still governed by phase contrast, as in conventional HREM, exhibiting contrast reversal with the change of focus and/or specimen thickness. Therefore, the bright fringes are not necessary representing the Al (or Ti) atomic planes.

The plasmon-loss electron image is the result of interference between electrons elastically scattered to different Bragg beams both before and after inelastic excitations. The coherent interference between these beams, producing lattice images, is possible because electrons inelastically scattered by the same crystal state (and therefore having the same energy loss and momentum transfer) are still coherent. Since there are many crystal states of different energies and momenta, the final image contrast is reduced due to the incoherent superposition of the electrons scattered by different crystal states.

Lattice images can also be formed by multiply scattered plasmon electrons. For energy losses smaller than about 200 eV in EELS spectra, the background is mainly dominated by multiple plasmon scattering. Figs. 9a and 9b compare the zero-loss and multiple plasmon-loss electron images of an Al/Ti interface. Fig. 9b was recorded by selecting the electrons with energy losses between 60–70 eV before the Al-$L_{2,3}$ edge. This part of the energy-loss spectrum contains the extended portion of the Ti-$M_{2,3}$ edge, resulting in stronger intensity at the Ti side. The Ti lattice fringes are also seen. In addition, an energy-selected image of the Al-L edge is shown in Fig. 9c. The poor signal-to-noise ratio in this image

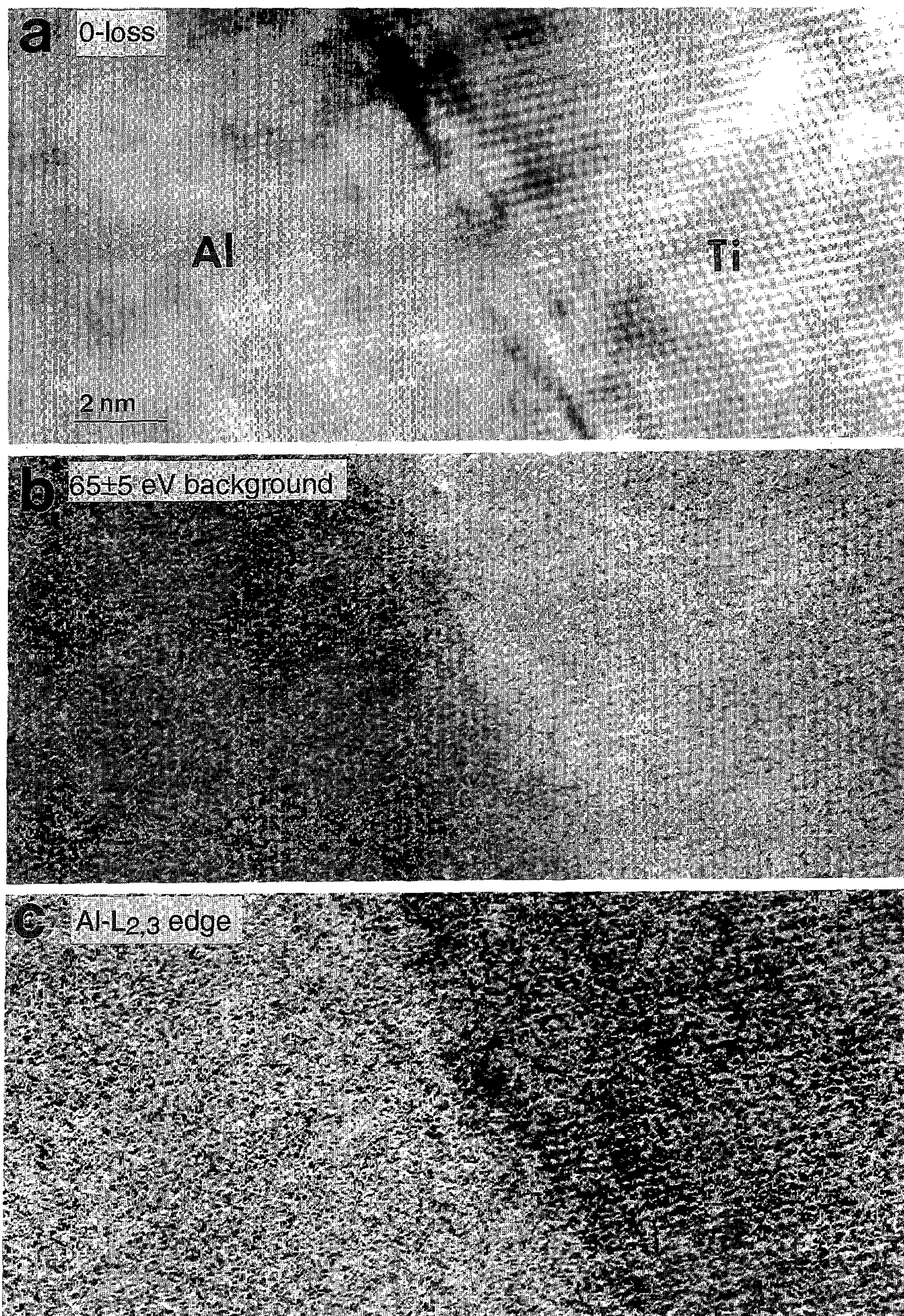

Fig. 9. (a) Zero-loss, (b) 65 eV EELS background loss and (c) background-subtracted Al-$L_{2,3}$ edge energy-selected HREM images of an Al/Ti (111) interface, after subtraction of background, showing the formation of lattice images by multiple plasmon-loss electrons. Energy window Δ = 10 eV. Beam azimuth $[1\bar{1}0]$.

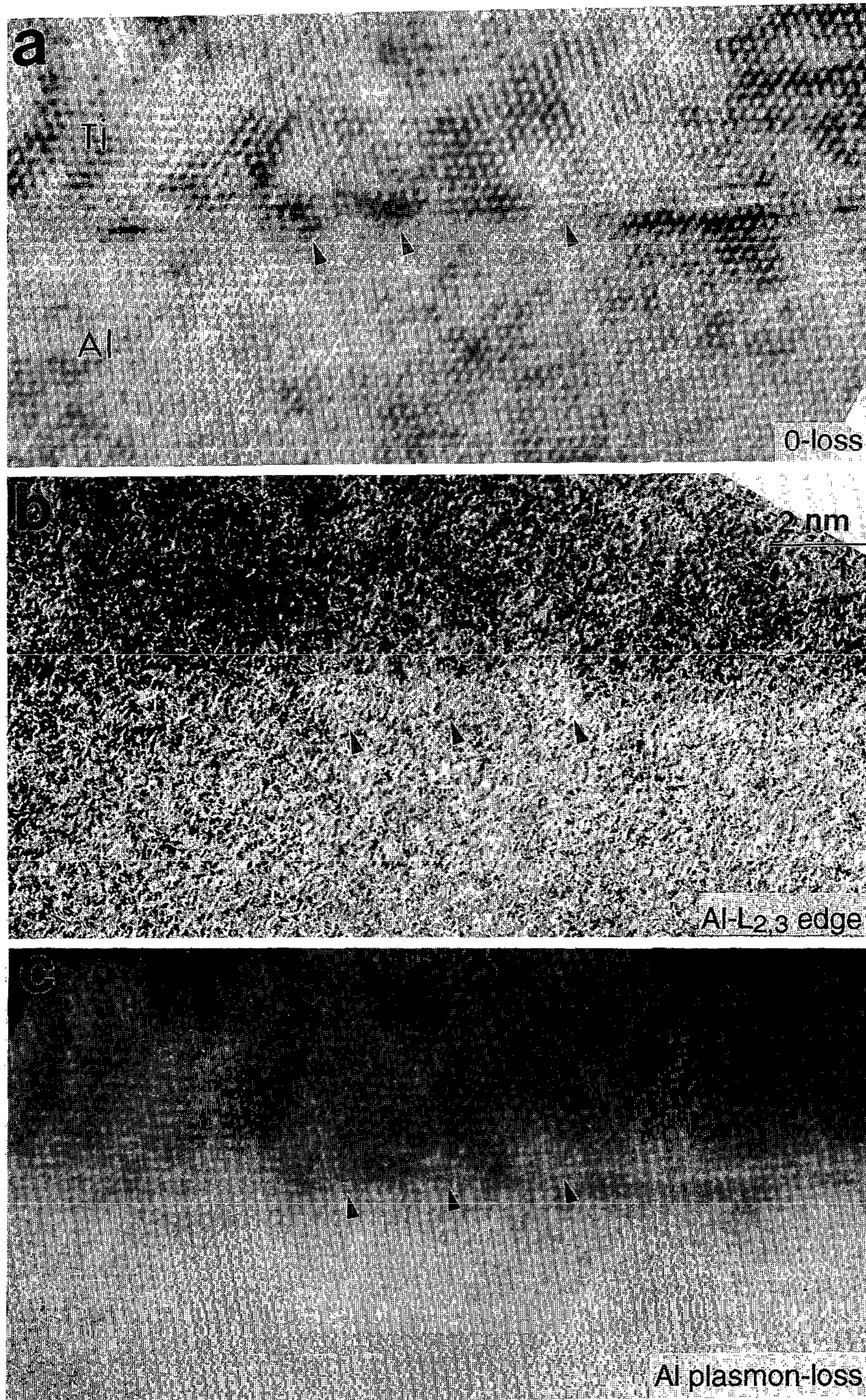

Fig. 10. (a) Zero-loss, (b) background-subtracted Al-$L_{2,3}$ edge and (c) 15 eV Al plasmon-loss energy-selected HREM images of an Al/Ti (111) interface. Crystal structure is clearly seen in the zero-loss image. Composition map is provided by both (b) and (c). Energy window $\Delta = 8$ eV. Beam azimuth $[1\bar{1}0]$. Data acquisition time 2 s.

results from the short acquisition time. In practice, specimen drift can be a serious problem, particularly at high-resolution imaging, if the acquisition time is long. Thus, the image acquisition has to be performed in a shortest possible time if one is looking for the highest spatial resolution.

In the multiple plasmon-loss electron image (Fig. 9b), the intensity at the Ti side is significantly stronger than that at the Al side. This observation may also be interpreted with the consideration of the electron stopping power, an average rate at which the electron energy decreases while transmitting the crystal. Since the stopping power increases with increasing atomic number [27], more electrons are expected to experience energy losses at the Ti side. Our observations in this Section have shown consistent results as reported by others [28–30].

3.6. Spatial resolution in energy-filtered composition-sensitive imaging

The energy-selected images using inelastically scattered electrons in the last few sections were taken with relatively longer acquisition periods (typically about 5–10 s) in order to improve the signal-to-noise ratio. Thus, the image contrast at the interface may be slightly smeared out by specimen drift. In order to get a better measurement of the spatial resolution obtained using the GIF system, the image acquisition time was reduced to 2 s. Fig. 10a is a zero-loss energy-filtered [110] HREM image of an Al/Ti multilayer interface. The interface is clean and structurally sharp with a width less than two atomic layers. Fig. 10b shows the corresponding energy-selected electron image of the Al-$L_{2,3}$ ionization edge. The chemical sharpness of the interface is seen directly. The arrowheads indicate a few places where higher Al concentrations are observed because of their stronger intensity in the Al-$L_{2,3}$ ionization edge image. These paired high-resolution structure and chemical images are very useful for unique determination of the local crystal structure and chemistry.

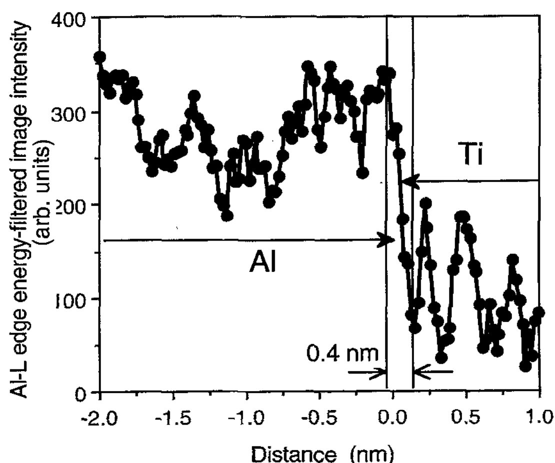

Fig. 11. An intensity line scan across the Al/Ti interface from the image recorded using the Al-$L_{2,3}$ edge energy-loss electrons (Fig. 10b), showing the spatial resolution obtained in core-loss electron imaging.

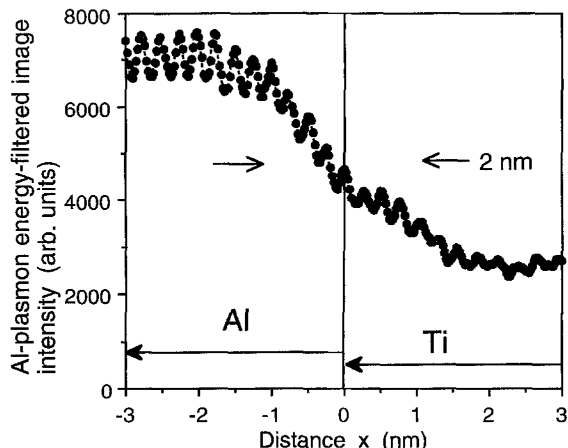

Fig. 12. An intensity line scan across the Al/Ti interface from the image recorded using the 15 eV Al plasmon-loss electron image (Fig. 10c), showing the dependence of inelastic absorption function on the impact distance x of the electron from the interface. This curve determines the spatial resolution of valence-loss electron imaging.

To see the spatial resolution obtained using the energy-filtering system, an intensity line scan across the Al/Ti interface is made and the result is averaged for a width of 50 pixels parallel to the interface. The intensity scan from the Al-$L_{2,3}$ edge energy-filtered image of Fig. 10b is shown in Fig. 11. Each dot in this figure is a pixel. The intensity variation from pixel to pixel is the statistical noise. But an average intensity drop between the Al and Ti sides is apparant. The Al concentration shows a sharp jump at the interface and a

spatial resolution of about 0.4 nm is obtained. With consideration the fact that the interface may not be absolutely monolayer sharp, the spatial resolution may be better than 0.4 nm. This value is consistent with the early studies of Mory et al. [31] who showed 0.4 nm spatial resolution from the energy-filtered images of U-$O_{4,5}$ edge with the use of single atom uranium specimen in STEM.

To estimate the spatial resolution of the plasmon-loss electron image (Fig. 10c), a line scan is made across the Al/Ti interface, and the result is shown in Fig. 12. The free oscillation in the intensity profile is due to the lattice fringes. The intensity profile drops within a distance of 2 nm around the interface. Thus, the spatial resolution is approximately 1.0 nm. This spatial resolution is determined by the non-localized scattering of valence electrons. A theoretical analysis will be provided in Section 4.2.

As chromatic aberration effect is concerned, it seems that the optimum spatial resolution is obtained with the use of a small width energy window, provided the signal-to-noise ratio is strong enough. In this case, the energy-selected ionization image is sensitive to specimen composition but it is not strictly the compositional image, at least for some elements whose near edge free structures are strongly affected by the solid state effect, such as O-K. This is because the quantification of specimen composition from the energy-selected ionization edge image depends on the integrated ionization cross-section $\sigma_A(\Delta)$ of the element. Unfortunately, $\sigma_A(\Delta)$ is, at least for some elements, strongly affected by the solid state effect if the integration window Δ is smaller than about 30 eV [32]. Therefore, for a general case, the energy-filtered ionization edge image should be referred to as composition-sensitive image rather than compositional image.

4. Theoretical interpretation

4.1. Localization effect in surface excitation

We now consider the interface excitation by an electron beam. Valence excitation spectra can be quantitatively simulated with the use of the dielectric response theory [33–35]. In this theory, an incident electron is treated as a particle that moves along a well defined path. This model holds as long as the changes of electron energy and momentum are small. In the general case, an interface is formed by two media with dielectric functions ε_1 and ε_2. The two media are assumed to be semi-infinity large and is separated by a sharp interface located at $x=0$. The incident electron is assumed to travel at a distance x_0 in medium ε_1 parallel to the interface. The energy loss of the electron is the work done by the induced charges distributed in the bulk and at the interface to slow down the electron motion. The energy-loss rate per unit distance is related to the excitation probability by

$$-\frac{dE}{dz}=\int_0^\infty d\omega\,\hbar\omega\frac{d^2P}{d\omega\,dz}. \qquad (5)$$

For simplicity, we use the non-relativistic dielectric response theory. The excitation probability of the valence band is [34,35]

$$\frac{d^2P}{dz\,d\omega}=\frac{e^2}{2\pi^2\varepsilon_0\hbar v^2}\left\{\text{Im}\left\{-\frac{1}{\varepsilon_1}\right\}\left[\ln\left(\frac{2\pi q_c v}{\omega}\right)-K_0\left(\frac{2\omega x_0}{v}\right)\right]+\text{Im}\left\{-\frac{2}{\varepsilon_1+\varepsilon_2}\right\}K_0\left(\frac{2\omega x_0}{v}\right)\right\}, \qquad (6a)$$

with

$$K_0\left(\frac{2\omega x_0}{v}\right)=\int_0^{2\pi q_c}du\frac{\exp\left\{-2\left[u^2+(\omega/v)^2\right]^{1/2}|x_0|\right\}}{\left[u^2+(\omega/v)^2\right]^{1/2}}, \qquad (6b)$$

where v is the electron velocity; e is the electron charge; q_c is the cut-off wave vector of valence losses; and ε_1 and ε_2 are the dielectric functions of media 1 and 2, respectively, which are assumed to be independent of the wave vector q. A rigorous form of Eq. (6a) with the inclusion of rela-

tivistic correction has been given by Garcia-Molina et al. [35]. In Eq. (6a), the first term is the excitation probability of the volume plasmon as a function of the incident electron impact distance from the interface. This term decreases as the electron approaches the interface. The second term is the excitation probability of the interface.

In the case of surface excitation, the excitation probability for an external beam case is obtained after substitutions of $\varepsilon_1 = 1$ and $\varepsilon_2 = \varepsilon$,

$$\frac{d^2P(x_0)}{dz\,d\omega} = \frac{e^2}{2\pi^2\varepsilon_0\hbar v^2}\mathrm{Im}\left\{-\frac{2}{\varepsilon+1}\right\}K_0\left(\frac{2\omega x_0}{v}\right), \tag{7}$$

for $x_0 > 0$. For an internal beam ($x_0 < 0$),

$$\frac{d^2P}{dz\,d\omega} = \frac{e^2}{2\pi^2\varepsilon_0\hbar v^2}\left\{\mathrm{Im}\left\{-\frac{1}{\varepsilon}\right\}\left[\ln\left(\frac{2\pi q_c v}{\omega}\right) - K_0\left(\frac{2\omega x_0}{v}\right)\right] + \mathrm{Im}\left\{-\frac{2}{\varepsilon+1}\right\}K_0\left(\frac{2\omega x_0}{v}\right)\right\}. \tag{8}$$

$\mathrm{Im}\{-1/\varepsilon\}$ and $\mathrm{Im}\{-2/(\varepsilon+1)\}$ are the volume and surface energy-loss functions, respectively. The inelastic absorption function is calculated by

$$\mu(x_0) = \frac{1}{\Lambda(x_0)} = \int_{\Delta}^{\infty} d\omega \frac{d^2P(x_0)}{dz\,d\omega}, \tag{9}$$

where Δ is the width of the energy-selecting slit.

Fig. 13 shows the calculated absorption function as a function of the electron beam impact distance from the MgO(100) surface. The solid and dash-dotted lines represent the excitation probabilities of the volume (VP) and surface plasmons (SP), respectively. The dashed line is the total excitation probability of the surface and volume plasmons. The excitation of the volume plasmon occurs only when the electrons penetrate deep into the crystal. The excitation of the surface plasmon occurs in a region about 1.5 nm from the surface. Only surface plasmon is excited if the electron is traveling outside of the crystal. It is apparent that the total absorption function experiences a sharp drop when the electron impact distance across the surface. The profile of the volume plasmon agrees very well with the observed curve shown in Fig. 4. This result will be explained in Section 4.3.

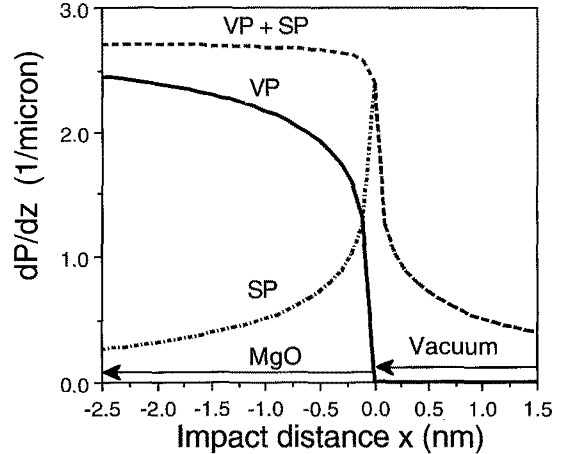

Fig. 13. Calculated absorption function $\mu = dP/dz$ across an MgO(100) surface, showing the dependence of the absorption function on the impact distance of the electron from the surface. $E_0 = 300$ keV, $q_c = 10$ nm^{-1}. SP: surface plasmon; VP: volume plasmon.

4.2. Spatial resolution in composition-sensitive imaging using valence-loss electrons

To provide a theoretical interpretation regarding the spatial resolution observed in the plasmon-loss electron image shown in Fig. 12, we now apply Eq. (6a) to calculate the intensity observed in the image across the Al–Ti interface. If the media on the both sides of the interface have the same thickness, the electron intensity inelastically scattered to an energy-loss range ΔE_1 to ΔE_2 ($\Delta = \Delta E_2 - \Delta E_1$) is proportional to

$$\mu = \frac{dP(x_0)}{dz} = \frac{e^2}{2\pi^2\varepsilon_0\hbar v^2}\int_{\omega_1}^{\omega_2} d\omega \left\{\mathrm{Im}\left\{-\frac{1}{\varepsilon_1}\right\} \times\left[\ln\left(\frac{2\pi q_c v}{\omega}\right) - K_0\left(\frac{2\omega x_0}{v}\right)\right] + \mathrm{Im}\left\{-\frac{2}{\varepsilon_1+\varepsilon_2}\right\}K_0\left(\frac{2\omega x_0}{v}\right)\right\}, \tag{10}$$

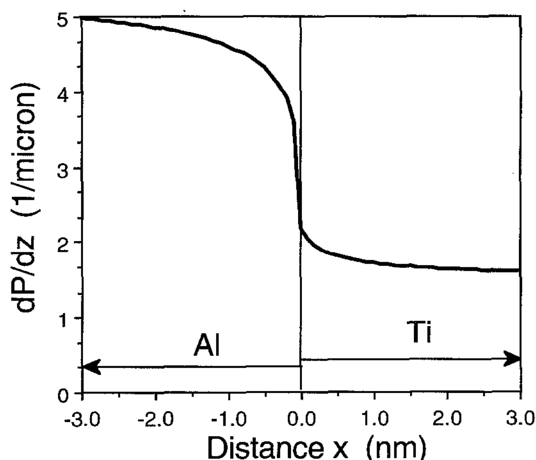

Fig. 14. Calculated absorption function across an Al/Ti interface, showing the dependence of the absorption function on the impact distance the electron from the interface. $E_0 = 300$ keV, $q_c = 10$ nm^{-1}. The interface position is indicated by a vertical line.

where $\omega_1 = \Delta E_1/\hbar$ and $\omega_2 = \Delta E_2/\hbar$. Fig. 14 shows the calculated curve of the integrated excitation probability given by Eq. (10) for the Al–Ti interface, where the energy window was selected to include the Al plasmon, $\Delta E_1 = 11$ eV and $\Delta E_2 = 18$ eV. The intensity drop at the interface is qualitatively in agreement with the experimental observation shown in Fig. 12. The spatial resolution is half of the width within which the intensity drops from the flat Al region to the flat Ti region. Although the interface was assumed to be chemically sharp in the calculation, the spatial resolution is limited to about 1 nm. This localization effect results in chemical ambiguity at the interface.

4.3. Classical model of interface excitation

From the discussion given above, there are two discrepancies between the observed and the calculated absorption functions across the interface. For the MgO surface, the observed absorption profile (Fig. 4) does not agree to the calculated one for the total valence losses (surface and volume) but the volume plasmon (Fig. 13). For the Al–Ti interface excitation, the gradient of the calculated curve (Fig. 14) is significantly larger than that of the observed one (Fig. 12). We now examine the model used for theoretical calculations in order to provide an interpretation.

The theory presented in Section 4.1 was derived based on a model which assumes that the two media are semi-infinity large and are separated by a sharp interface. For a thin foil of typical thickness about 20 nm used for surface profile HREM imaging, however, the infinitely-large surface (parallel to the electron beam) model fails. Thus, the model has over-estimated the contribution made by the surface excitation. In this case, the valence excitation is dominated by volume component. This is the reason that the calculated volume plasmon profile agrees well with the experimentally observed curve.

In the theoretical calculation, the interface is considered as an ideal two-dimensional plane without thickness. The induced charges produced by the incident electron in the media are distributed on this plane of zero thickness. In atomic dimensions, however, such a plane does not exist and the surface charges are distributed within about 0.5 nm from the top layer. In addition, the theoretical calculation has ignored the dispersion relation of the dielectric function by assuming that ε is independent of wave vector q. All these approximations have over estimated the contribution made by surface excitation when the electron impact distance approaches zero, resulting in the sharp drop of the calculated curve at $x = 0$.

5. Summary

In this paper, we have shown some characteristics of energy-filtered HREM for surface and interface studies. Energy-selected electron images can provide both structural and chemical information with high resolution. Zero-loss selected HREM images exhibit significantly increased image contrast in comparison to the unfiltered images, particularly for thicker specimens. From the zero-loss image, the inelastic mean-free-path length of MgO at 300 kV is determined as $\Lambda \approx 181$ nm.

Localization effect of valence losses has been considered in the energy-selected MgO(100) sur-

face profile electron images, indicating the decrease of the inelastic absorption function when the electron impact distance approaches the surface. This result has been interpreted using the calculated result of dielectric response theory for surface excitation.

High-resolution chemical-sensitive imaging using core-shell loss electrons in transmission electron microscopy (TEM) has been demonstrated in the studies of Al/Ti multilayer thin films. A spatial resolution of ~ 0.4 nm has been obtained across the interface. Specimen chemical information can be provided by the Gatan imaging filtering system at an acquisition time much shorter than the acquisition time using energy-dispersive X-ray spectroscopy. It has been shown that the spatial resolution of the energy-selected ionization edge electron image is dominated by the signal-to-noise ratio; the signal localization, as long as it comes from inner-shell excitation, has little effect. Thus, an ionization edge, located at lower energy-loss region with strong intensity, is recommended for chemical-sensitive imaging. However, cautions must be exercised in the subtraction of the background.

Composition-sensitive imaging using plasmon-loss electrons is also feasible, and a spatial resolution better than 1.0 nm has been obtained. The signal-to-noise ratio is usually strong enough to image fine details in the specimen. For interfaces, the inelastic absorption function depends sensitively on the impact distance of the electron from the interface. This profile has been measured experimentally, and the result has been compared with the calculation of the dielectric response theory.

Lattice images can be formed by plasmon-loss and multiple plasmon-loss electrons. The image is the result of interference between electrons elastically scattered to different Bragg beams both before and after inelastic excitations. The coherent interference between these beams is possible because electrons inelastically scattered by the same crystal state are coherent. Thus, the phase contrast mechanism holds. However, the image contrast is poor because there are many crystal states and the scattering between these states is incoherent. Thus, the observed image is an incoherent superposition of the electrons scattered by different crystal states.

Acknowledgements

Thanks to Dr. D. van Heerden for kindly providing the Al/Ti multilayer specimen. Thanks to Drs. B. Hockey and J. Weissmuller for comments. In this paper, reference to commercial equipment does not imply NIST endorsement.

References

[1] P. Buseck, J.M. Cowley and L. Eyring, Eds., High-Resolution Transmission Electron Microscopy (Oxford University Press, Oxford, 1989).
[2] J.J. Hu, F.H. Li and H.F. Fan, Ultramicroscopy 41 (1992) 387.
[3] R. Castaing and L. Henry, C.R. Acad. Sci. (Paris) B 255 (1962) 76.
[4] S. Senoussi, L. Henry and R. Castaing, J. Microscopie 11 (1971) 19.
[5] L. Reimer, A. Bakenfelder, I. Fromm, R. Rennekamp and M. Ross-Messemer, EMSA Bull. 20 (1990) 73.
[6] L. Reimer, I. Fromm and I. Naundorf, Ultramicroscopy 32 (1990) 80.
[7] L. Reimer, I. Fromm and R. Rennekamp, Ultramicroscopy 24 (1988) 339.
[8] A. Berger, J. Mayer and H. Kohl, Ultramicroscopy 55 (1994) 101.
[9] H. Shuman, C.F. Chang and A.P. Somlyo, Ultramicroscopy 19 (1986) 121.
[10] O.L. Krivanek, A.J. Gubbens and N. Dellby, Microsc. Microanal. Microstruct. 2 (1991) 315.
[11] Z.L. Wang, Elastic and Inelastic Scattering in Electron Diffraction and Imaging (Plenum, New York, 1995) chs. 6–15.
[12] C. Colliex, PhD Thesis, 1970.
[13] L. Reimer and M. Ross-Messemer, J. Microscopy 155 (1988) 169; 159 (1989) 143.
[14] A. Bakenfelder, I. Fromm, L. Reimer and R. Rennekamp, J. Microscopy 159 (1989) 161.
[15] M.J. Whelan, J. Phys. C 9 (1976) L195.
[16] T. Tanji, K. Urata, K. Ishizuka, Q. Ru and A. Tonomura, Ultramicroscopy 49 (1993) 259.
[17] D.E. Newbury, Microscopy: The Key Research Tool 22 (1992) 11.
[18] M. El Gomati, I. Barkshire, J.C. Greenwood, P.G. Kenny, R. Roberts and M. Prutton, Microscopy: The Key Research Tool 22 (1992) 29.
[19] S.J. Pennycook, Microscopy: The Key Research Tool 22 (1992) 51.
[20] J. Bentley, K.B. Alexander and Z.L. Wang, in: Proc. 12th Int. Congr. for Electron Microscopy, Seattle, Vol. 2 (San Francisco Press, San Francisco, 1990) p. 400.

[21] C. Colliex, Ultramicroscopy 18 (1985) 131.
[22] R.D. Leapman and J.A. Hunt, Microscopy: The Key Research Tool 22 (1992) 39.
[23] D. Shechtman, D. van Heerden and D. Josell, Mater. Lett. 20 (1994) 329.
[24] A. Howie, Proc. Roy. Soc. (London) 271 (1963) 268.
[25] Z.L. Wang and J. Bentley, Microsc. Microstruct. Microanal. 2 (1992) 569.
[26] O.L. Krivanek, C.C. Ahn and G.J. Wood, Ultramicroscopy 33 (1990) 177.
[27] R.H. Ritchie and A. Howie, Phil. Mag. 36 (1977) 463.
[28] N. Ajika, H. Hashimoto, K. Yamaguchi and E. Endoh, Jpn. J. Appl. Phys. 24 (1985) L41.
[29] H. Hashimoto, Y. Makita and N. Nagaoko, in: Proc. 50th Annual EMSA Meeting, 1992, p. 1194.
[30] A.J. Craven and C. Colliex, J. Microsc. Spectrosc. Electron. 2 (1977) 511.
[31] C. Mory, H. Kohl, M. Tencé and C. Colliex, Ultramicroscopy 37 (1991) 191.
[32] P. Rez, X. Weng and H. Ma, Microsc. Microstruct. Microanal. 2 (1991) 143.
[33] A. Howie, Ultramicroscopy 11 (1983) 141.
[34] A. Howie, in: Surface and Interface Characterization by Electron Optical Methods, Eds. A. Howie and U. Valdre (Plenum, New York, 1988).
[35] R. Garcia-Molina, A. Gras-Marti, A. Howie and R.H. Ritchie, J. Phys. C: Solid State Phys. 18 (1985) 5335.